A μNMR CMOS Transceiver Using a Butterfly-Coil Input for Integration With a Digital Microfluidic Device Inside a Portable Magnet

Ka-Meng Lei, *Student Member, IEEE*, Pui-In Mak, *Senior Member, IEEE*,
Man-Kay Law, *Member, IEEE*, and Rui P. Martins, *Fellow, IEEE*

Abstract—This paper describes a 20 MHz micro-nuclear magnetic resonance (μNMR) transceiver (TRX) featuring a butterfly-coil input for chemical/biological assays. It enables integration with a 2D multi-electrode digital microfluidic (DMF) device inside a space-limited portable magnet (0.46 T, 1.25 kg), making multi-sample management compatible with μNMR measurements, and supporting electronic automation. The transmitter (TX) incorporates a pulse-sequence synthesizer followed by an inverter-based power amplifier (PA), to emit the exciting pulses for magnetizing the protons of the samples. For the receiver (RX), it is headed by a multi-stage low-noise amplifier (LNA) using NMOS-PMOS-complementary differential pairs, achieving a sub-nV/$\sqrt{}$Hz input-referred noise at low power. Sixth-order Butterworth low-pass filters constitute the core of the RX I/Q baseband. Their source-follower-based topology allows fast and coherent scaling of all poles by the bias current, reducing the dead-time of the RX for better sensitivity. Fabricated in 0.18 μm CMOS, the TRX occupies a die area of 2.1 mm^2, consumes 6.6/23.7 mW of power in the TX/RX mode, and demonstrates the feasibility of electronic-automated biological (avidin) and chemical (CuSO$_4$) assays achieving a detection limit on avidin of 0.2 pmol.

Index Terms—Avidin, biological, baseband, chemical, CMOS, digital microfluidic (DMF), electronic automation, filter, power amplifier (PA), low-noise amplifier (LNA), magnetic sensing, nuclear magnetic resonance (NMR), point-of-care, radio frequency (RF), receiver (RX), transceiver (TRX), transmitter (TX).

I. INTRODUCTION

THERE has been a global health challenge to improve the disease management in rural areas and developing countries with limited resources [1]–[3]. According to the

World Health Organization (WHO), lower-income countries suffer from "diseases of poverty" including HIV, tuberculosis, and malaria, where prompt diagnosis can inhibit their outbreak at the community level. Standard tests such as qualitative polymerase chain reaction (for DNA) and enzyme-linked immunosorbent assay (for antibodies/antigens), centralized in clinical laboratories and implemented by trained technicians, are very costly and time-consuming. In this respect, decentralized Point-of-Care (POC) devices with minimal sample purification and processing are of great interest to replace benchtop laboratory equipment [4]. These POC devices facilitate early screening of diseases even in the outdoors, rendering it a prominent diagnostic solution in developing countries. Ideally, these POC diagnostic platforms should match with the ASSURED (Affordable, Sensitive, Specific, User-friendly, Robust and rapid, Equipment-free, Delivered) guidelines from WHO.

A wide variety of portable and selective diagnostic tools are currently available in CMOS. They can be categorized according to their sensing mechanisms. It is possible to read the electrical properties of the medium such as charge flows (currents) [5] or impedance (resistance and/or capacitance) [6], [7]. This technique offers label-free and direct electrical detection for the biomolecule targets of interest. Yet, the sensing electrodes (e.g., gold layer) have a recognition probe layer deposited on them to selectively detect the target [8]. This probe immobilization procedure stiffens the manufacturing process and raises its cost, plus the CMOS chip is not reusable, as its sensing electrode must interface directly with the sample. Alternatively, there have been efforts to miniaturize benchtop fluorimeters into CMOS to detect visible-range fluorescent light [9], [10]. Labeled by the fluorescent dyes such as Cy3 and Cy5, the fluorimeters can detect the target analyte from their florescent signals after exposure to an incident excitation light. Although this method does not obviate probe immobilization process, the CMOS chip can be reused because there is no direct contact. However, the external modules (i.e., optical filter) still challenge the assembly of the device in a portable scale. Using magnetic beads, the quasi-labeling-free [11] magnetic sensing can be utilized to identify the wanted targets. Upon being captured by the targets, the magnetic beads labeled with probe alter the magnetic properties

TABLE I
SUMMARY OF DIFFERENT CMOS-BASED BIO-SENSING POC SYSTEMS

	Impedometric/ Amperometric	Fluorescent	Magnetic	NMR
Primary Mechanism	Electrical Properties	Optical Properties	Magnetic Properties	Nuclei Spinning (RF Magnetic Field)
Probe Immobilization	Yes	Yes	Yes	No
Labeling	Label-Free	Labeling-Based	Quasi-Labeling-Free	Quasi-Labeling-Free
Contact between CMOS Die and Sample	Yes	No	No	No

in the proximity of the targets. A magnetic-sensitive element, such as a Hall sensor [12], an LC-oscillator [13], and giant magneto-resistive spin-valve sensors [14], can detect this discrepancy. When compared with impedometry, although probe-immobilization is still ineluctable, the recognition layer realized without affecting the CMOS chip enhances its reusability. Other sensing mechanisms such as micro-cantilever [15] and ion-selected field-effect transistor [16] are also available for target identification in CMOS.

Nuclear magnetic resonance (NMR) is a promising alternative that explores the magnetic properties at the atomic level. Its advantages are no direct contact (i.e., non-invasive) with the sample, and probe-decorated magnetic nanoparticles (MNPs) can be used for selective target-quantifying. Furthermore, NMR sensing is free from probe-immobilization on the surface, allowing various assays on different targets with the same readout circuit for higher throughput. Hence, NMR is unique among various bio-sensing mechanisms albeit it is also detecting the magnetic properties of the samples. First reported in 2001, detections of a wide range of unprocessed targets such as DNA [17], proteins [18], viruses [19] and telomerase (for cancer study) [20] using NMR-based bio-sensing methods have been reported by evaluating the spin–spin relaxation time (T_2) of the protons. Yet, limited by the sensitivity of their systems, the NMR-signal detection still relied on benchtop equipment, hindering their applicability to POC diagnosis. Recently, pioneering micro-NMR (μNMR) systems aiming for weight and size miniaturization have been demonstrated in CMOS for applications in relaxometry (nuclei relaxation times) [21]–[23] and spectroscopy (NMR spectrum) [24]. With advanced circuit techniques to lessen the penalty of signal attenuation induced by the compact magnet (<7.3 kg), these μNMR systems offer a trailblazing sensing method befitting more the POC diagnosis (Table I). Yet, it is still not possible to pipeline multiple samples to the μNMR sensing region for higher throughput and real-time result comparison (e.g., concentration of the analytes) due to the small inner space and limited NMR sensing region of a portable magnet (0.46 T, 1.25 kg). In this respect, the biocompatible and reconfigurable digital microfluidic (DMF) device [25] is attractive for integration with the μNMR system. DMF can cope with 2D droplet-sample operation (e.g., transportation, mixing and splitting) accurately by modulating the surface tension of the DMF electrodes under the principle of electrowetting-on-dielectric (EWOD) [26], [27]. This paper
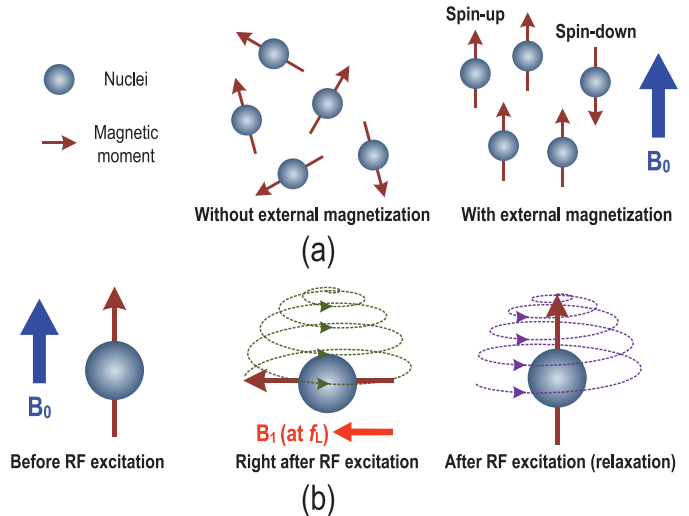

Fig. 1. (a) Macroscopic view of the non-zero spin nuclei. With an external magnetic field B_0 applied to the nuclei, part of them will align with this magnetic field. (b) The effect of RF excitation on the nucleus under magnetization. When excited by the RF magnetic field at Larmor frequency, the nuclei precess around the magnetization. After this magnetization, the nuclei still resonate and return to the equilibrium, with this relaxation recorded and analyzed.

reports a CMOS butterfly-coil-input transceiver (TRX) [28] for relaxometry (T_2) measurements inside a portable magnet. Co-operating with the DMF device, multiple samples can time-share one NMR sensing site that aligns with the TRX's butterfly coil, enhancing throughput and repeatability, while averting the risks of defilement of the assays.

Section II overviews the principle of NMR, and the key features of our proposed μNMR system. Section III exhibits in detail the design and implementation of the main building blocks. Section IV summarizes and discusses the experimental results. Finally, Section V draws the conclusions.

II. PRINCIPLE OF NMR AND SYSTEM OVERVIEW

The principle of NMR is the exchange of energy between the RF magnetic field and precession of the non-zero spin nuclei. Under the magnetization with an external magnetic field B_0, parts of the nuclei align with this external magnetic field and have a spin-up state while the others have a spin-down state [Fig. 1(a)]. As the population ratio between the protons with spin-up and spin-down state is proportional to B_0 and this difference determines the amplitude of the NMR signal, there exists a tradeoff between the portability and
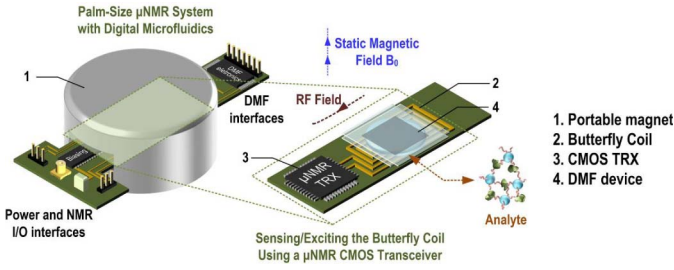
Fig. 2.   Portable electronic-automated μNMR system. It features a CMOS TRX and a PCB-based butterfly-coil inside the magnet to transduce between magnetic and voltage signals. The analyte is placed inside a glass-substrate digital microfluidic (DMF) device atop the butterfly-coil for sample management (only 1 electrode is shown for simplicity).

Fig. 3.   Three-phase operation of the μNMR system: setup, samples preparation, and analysis.

sensitivity of the system. With an RF magnetic field B_1 orthogonal to B_0 applied on the nuclei, they precess and tip away in the direction of bulk magnetization [Fig. 1(b)]. The nuclei only accept RF excitation at Larmor frequency, defined as

$$f_L = \gamma B_0 \qquad (1)$$

with the gyromagnetic ratio of the nuclei γ. For a 0.46 T magnet, the f_L of ^{1}H is $\sim$ 20 MHz. The nuclei do not precess if there is a mismatch on the excitation frequency and f_L. After tipping the nuclei 90° from the direction of bulk magnetization, the excitation is turned off. Still, the nuclei will resonate and decay exponentially with spin–spin relaxation time T_2 at f_L. This T_2 reveals the magnetic field information across the nuclei. Unfortunately, the unavoidable inhomogeneity of B_0 from the portable magnet causes spatial variation on the precession rate of the nuclei, thus the T_2 decays at a much faster rate T_2^*. This blemish hinders the measurement on original T_2. To surmount this, the spin-echo technique such as the Carr–Purcell–Meiboom–Gill (CPMG) pulse sequence can be utilized to refocus this dephasing effect on the nuclei by flipping the nuclei 180° with interval τ, thus the spins are maximized again from B_0 inhomogeneity [29], [30]. The envelope of the echoes responses allows the derivation of the resulting T_2 with the following mathematical expression:

$$A[n] = A_0 e^{-\frac{n\tau}{T_2}} \qquad (2)$$

with the echoes amplitude for nth echoes $A[n]$ and the initial amplitude A_0.

The μNMR system developed here combines relaxometry measurement and sample management in a handheld scale. As shown in Fig. 2, there are four major parts: 1) a portable magnet for magnetizing the nuclei; 2) a PCB-based butterfly-coil for transduction between magnetic fields from the nuclei and electrical RF signals for the TRX, inside the space-limited magnet; 3) a CMOS TRX to excite the nuclei with specific pulses sequences and collect their responses; and 4) a DMF device for sample management. Its operation involves three phases: setup, samples preparation, and analysis (Fig. 3). Before the experiment, all of the samples under assay are preloaded into the DMF device. Frequency matching requires magnetic field calibration. This obviates the challenge from ambient temperature variation and secures the function of
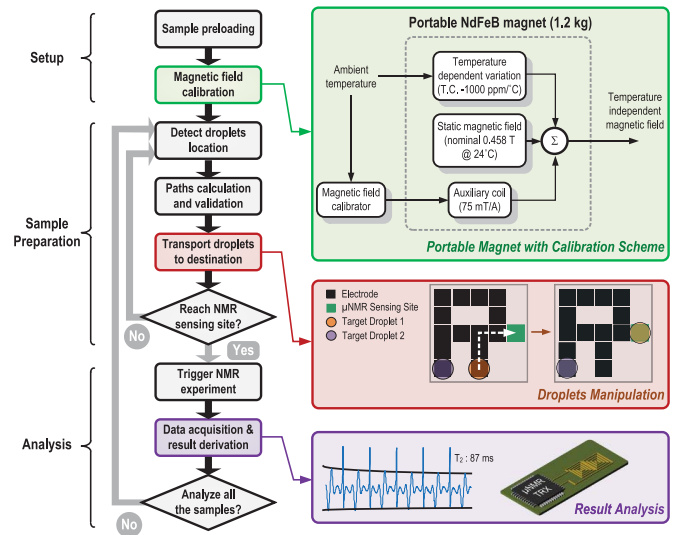
the μNMR assay. Then, the DMF device scans and delivers, individually, the samples to the μNMR sensing site, with closed-loop automation, thus tracking the experimental status. Upon arrival, with the μNMR assay triggered and the CMOS TRX taking results, a customized software program analyses and performs target identification. For multi-sample analysis, the DMF device keeps transporting the samples to the μNMR sensing site for assay. These modules cooperate in a closed-loop manner to culminate in a POC device capable of identify analyte inside μL-droplets with multi-step reaction and timing control.

III. Design and Implementation

The electrical schematics of the system are illustrated in Fig. 4, which includes a butterfly-coil, a CMOS μNMR TRX, a DMF device with its DMF electronic, and a FPGA with ADCs that link up the system with a computer for easy execution and upgrade of protocols written in software. One electrode has the butterfly-coil placed underneath as the μNMR sensing site. The design of the μNMR TRX focuses on the TX's flexibility and power efficiency, RX's input-referred noise, and the interface with its butterfly-coil. Their design and implementation will follow next.

A. μNMR TRX

For μNMR excitation, a specific CPMG pulse sequence at f_L ($\sim$ 20 MHz) is required to apply on the sample to precess the protons and refocus the incoherent magnetization across the samples. To realize this, we utilize a TX consisting of a pulse-sequence synthesizer (Fig. 5) and a switching power amplifier (PA). An external signal generator LO_{ref} feeds the TX with a frequency 4x the f_L, and the frequency dividers generate a 4-phase LO matched with f_L, with its output serving as excitation pulses, as well as the LO signal for the quadrature mixers in the RX. This scheme allows the RX and TX to share the LO circuitry and ease the synchronization of
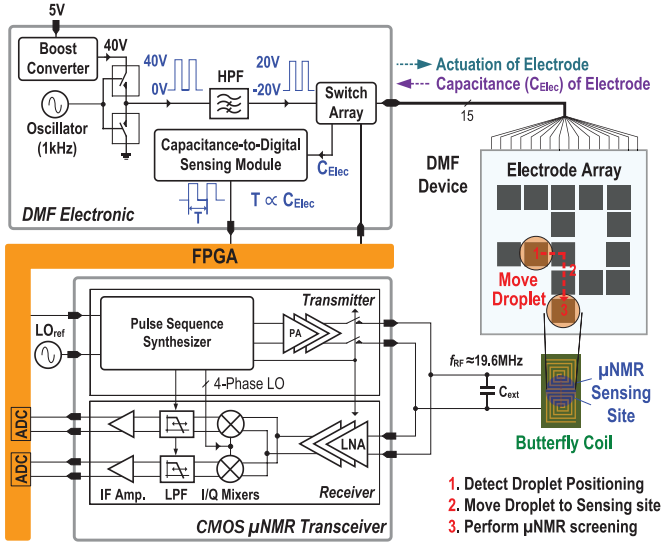
Fig. 4. Block diagram of the μNMR TRX cooperated with the DMF device. It includes a CMOS μNMR TRX with a butterfly-coil input, a DMF device, and a DMF electronic. An electrode has the butterfly-coil placed underneath for performing μNMR assays. A FPGA connected to a computer coordinates the hardware.
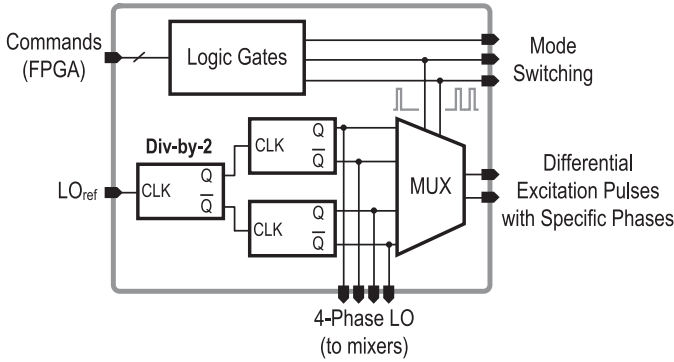

Fig. 5. Pulse-sequence synthesizer. FPGA commands control the logic gates to master the start and duration of the excitation signals with different phases as well as the switching between TX and RX modes.

their signals. Compared with the case of feeding an external LO at 2x f_L, the use of 4x f_L secures an accurate phase over process, voltage, and temperature variations. The logic gates mastered by the command from the FPGA flexibly generate the control signals with specific pulse width and interval for the switches of the whole TRX and multiplexer (MUX). The MUX governs the excitation signals delivered to the subsequent PA and butterfly-coil (Fig. 6). The PA is made of tapped inverter chains to ensure a high dynamic power efficiency when driving up the butterfly-coil to excite the protons.

After the excitation pulses, the same butterfly-coil picks-up the magnetic field produced from the nuclei spin. A capacitor C_{ext} is placed in parallel with the butterfly-coil to form a LC resonator at f_L to achieve passive amplification with gain of $\sqrt{Q^2 + 1}$, with the quality factor of the coil Q [21]. This scheme is feasible attributed to the narrowband behavior of the NMR signals (<5 kHz for this platform). Afterwards,
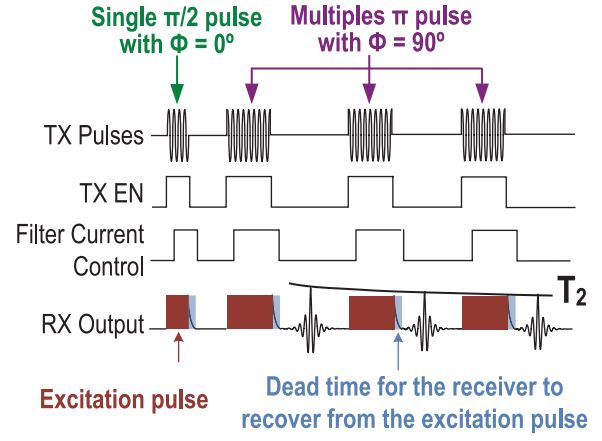

Fig. 6. The μNMR pulse sequence. It includes the CPMG pulse, filter current control, and μNMR output signal where the dead-time of the RX is shown.

TABLE II
SIMULATED NOISE SUMMARY OF THE LNA

		Input-Referred Noise (nV/√Hz)	Noise Contribution
1st stage LNA	PMOS pairs	0.30	22.76%
	NMOS pairs	0.41	42.35%
Thermal Noise from Back-End (via, polysilicon, metal)		0.36	32.91%
Others (2nd- and 3rd-stage LNAs)		0.09	1.88%
Total noise for the RF Stage		0.63	100%

this diminutive signal (< 1 μV) is recorded by the RX. A multi-stage NMOS-PMOS complementary differential-pair low-noise amplifier (LNA) heads the RX to maximize its sensitivity and to reject common-mode noise [Fig. 7(a)]. The input-referred noise for this LNA (single stage) is

$$\overline{v_{noise,LNA}^2} = \frac{8kT\gamma}{g_{M1} + g_{M3}} \tag{3}$$

with the Boltzmann constant k, the temperature in Kelvin T, noise coefficient of MOSFET γ (assuming the same γ for PMOS and NMOS). g_{M1} (M$_1$) and g_{M3} (M$_3$) are the transconductances assuming matched input pairs (i.e., M$_1$ = M$_2$ and M$_3$ = M$_4$). When compared to PMOS/NMOS-only input stage where the loads (either active or resistive) inevitably contribute with noise to the output, $\overline{v_{noise,LNA}^2}$ of this current-reuse topology (simulated: 0.51 nV/$\sqrt{}$Hz) can be reduced more effectively by raising the bias current (i.e., higher g_{M1} and g_{M3}). This topology usually suffers from limited voltage headroom since both M$_1$ (M$_2$) and M$_3$ (M$_4$) concurrently bound the input and output voltages. Nevertheless, ascribed to the fixed input bias (0.9 V) and tiny differential μNMR voltages, this topology particularly suits μNMR sensing. To reduce the substrate coupling noise from the digital circuits of the TX, the LNA is isolated from the p-type substrate by the deep N-well. Three stages of this amplifier are cascaded to achieve a gain of 87.6 dB with an overall simulated input-referred noise of 0.63 nV/$\sqrt{}$Hz, dominated by the forefront LNA (Table II).
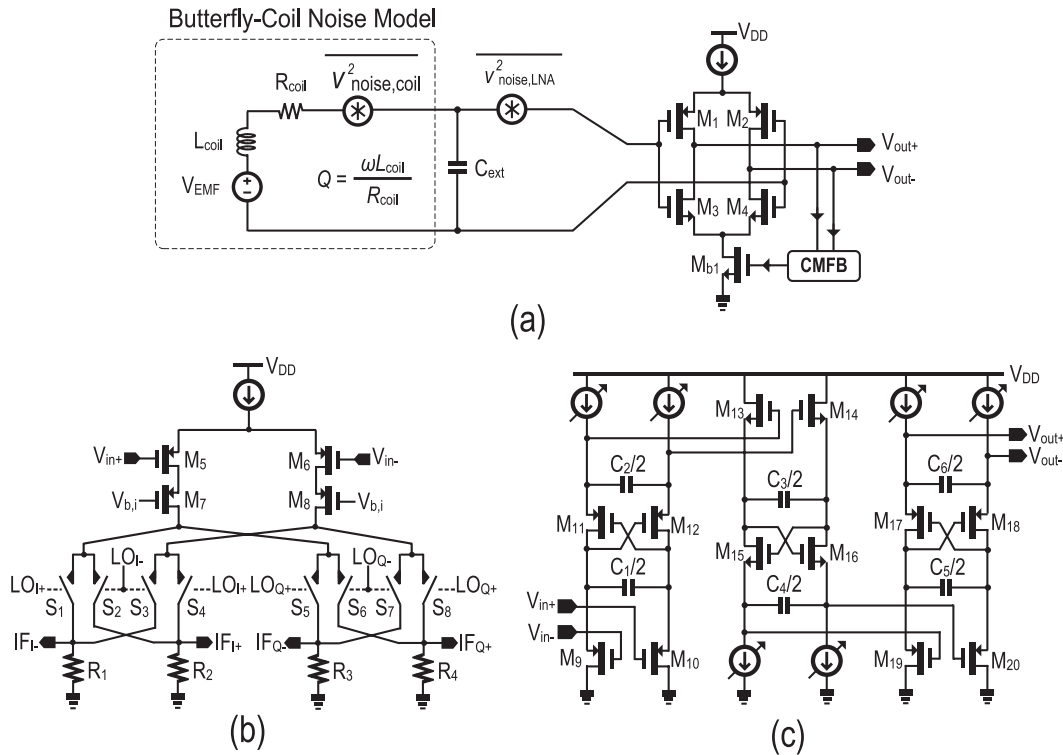
Fig. 7.   (a) Butterfly-coil-input LNA and its noise model. (b) Double-balance quadrature mixer with RF-sharing stage. (c) Source-follower-based tunable-bandwidth LPF.

The stages are AC-coupled to avoid the dc-offset of the LNA from saturating the RX.

Subsequent to the LNA, a double-balanced quadrature mixer based on the Gilbert cell [Fig. 7(b)] is employed to down-convert the RF signal to the baseband (bandwidth <5 kHz), whereas the quadrature signals can be processed at the software level to reject the image noise. This active mixer provides additional gain (12 dB), relaxing the noise requirement of the subsequent stages. The RF-sharing stage (M_5 and M_6) improves the I/Q matching and the cascode transistors (M_7 and M_8) improve the isolation between the ports. The downconversion is accomplished by the switches (S_1 to S_8), which are controlled by the square-LO from the TX for better noise performance. To prevent the hard-switching interference affecting other sensitive circuits, all transistors in this mixer (including the switches) are PMOS with individual N-well. As the RX only has to process a single tone signal at f_L, typical linearity indicators such as IIP3 cannot fully reflect its performance. Since only the amplitudes of the signals influence the relaxometry, the distortion on the downconverted monotone signals is critical for the RX design. From the simulations, for an input voltage amplitude of interest (<100 mV$_{pp}$) the third harmonic of the mixer is 40 dB below the fundamental signal [Fig. 8(a)]. In terms of distortion, the mixer has a total harmonic distortion (THD) below 1% (assuming the high-frequency mixing product is irrelevant) for an input voltage within 100 mV$_{pp}$, facilitating the consummation of frequency downconversion for the NMR signals [Fig. 8(b)].

A baseband LPF is essential to remove the high-frequency mixing products as well as the out-of-band noises of the
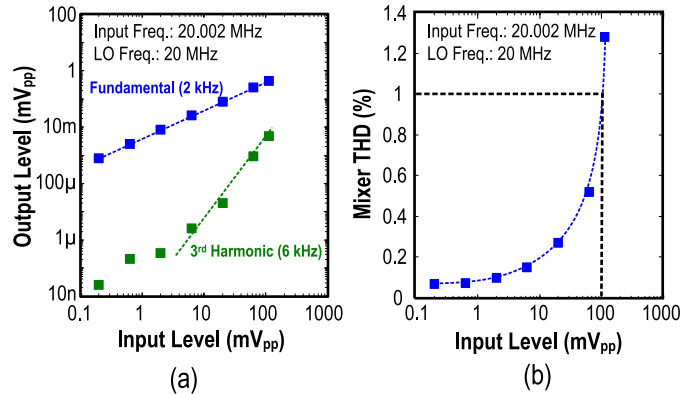

Fig. 8.   Simulation results of the mixer with LO = 20 MHz and input frequency = 20.002 MHz (i.e., IF = 2 kHz): (a) Output against input for fundamental and 3rd harmonic. (b) THD of the mixer at different input amplitudes.

signals after mixing. Two 6th-order Butterworth I/Q LPFs are implemented by cascading three source-follower-based Biquads [Fig. 7(c)]. Such Biquad topology is area-efficient as it can realize poles at low frequency by limiting the transconductance of the transistors, thereby averting large capacitors [31], [32]. Furthermore, it is power-efficient as it does not entail power-hungry operational amplifiers, and is capable of synthesizing complex poles in a single branch by using a transistorized positive feedback (e.g., M_{11} and M_{12}), which also benefits the linearity [31]. The change on bias current (i.e., transconductance) easily tunes its bandwidth (BW), preserving its Butterworth response against BW variations,
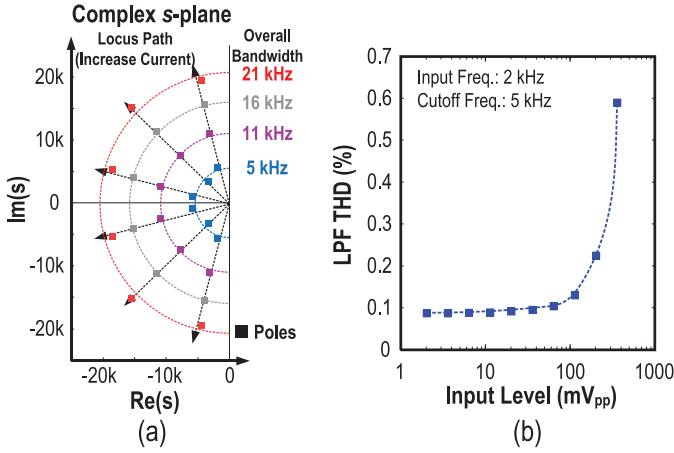
Fig. 9. (a) Simulated pole plot of the LPF. The 6th-order LPF implements a Butterworth filter (poles form a semicircle) with various cutoff frequencies obtained by changing only their bias currents. (b) Simulated THD of the LPF with an input frequency of 2 kHz and a cutoff frequency of 5 kHz for different input levels.

i.e. the poles form a semi-circle on the s-plane [Fig. 9(a)]. Similar to the mixer, the simulated THD of the LPF is within 1% for an input voltage within 400 mV$_{pp}$ [Fig. 9(b)]. The simulated integrated input-referred noise (0.1 to 100 kHz) of the LPF is 177.6 μV and it is designed with a power consumption of 212.4 nW per channel. The total capacitance of the LPF (per channel) is 49.2 pF. The figure-of-merit of the LPF is 128 fJ at a cutoff frequency (f$_{-3dB}$) of 5 kHz and is comparable to the state-of-the-art [32].

Theoretically, f$_{-3dB}$ should match with the BW of the signal (i.e., 5 kHz). Yet, the exciting pulses from TX will saturate the RX, in particular in the LPF as it has a slow recovery time attributed to the low f$_{-3dB}$. This dead-time (t_{dead}), which is dominated by the LPF and inversely proportional to its f$_{-3dB}$, ineluctably limits the shortest interval between the echoes of the CPMG pulses and hence the number of achievable echoes within the echoes train. For the samples with short T_2, t_{dead} limits the sensitivity of the experiment [33]. To minimize t_{dead}, a dynamic-baseband-BW tuning scheme (Fig. 6) is applied for the source-follower-based LPF. It leverages the compromise between fast recovery time from the excitation pulses in the TX mode, and minimum BW in the RX mode to reduce the in-band noise. The TX signals dynamically tune the LPF's bias current, slightly delayed from the exciting pulses for fully recovering. After the exciting pulses, the LPF's BW returns to low for higher rejection of the out-of-band noise. The simulated input-referred noise of the overall RX is 0.92 nV/√Hz before image noise rejection. Operated by batteries, the entire TRX powers down automatically when idling.

B. Portable Magnet and RF Coil Co-Design

The source of the magnetization is a portable magnet as its miniaturized size can match with the requirements of POC applications. This magnet, while with a coarser resolution when compared with the superconducting magnet, is adequate for relaxometry with the inhomogeneity recovered by CPMG pulse sequences. From (1), the f_L of the protons shifts with

the temperature dependent B_0 (T.C. -1000 ppm/K), thus f_L shifts with temperature correspondingly. Without calibration, LO frequency deviation from f_L will paralyze the system due to improper excitation frequency on the nuclei. To resolve this, we use a magnetic-field calibrator consisting of a temperature sensor and a current driver, as shown in the inset of Fig. 3. A temperature sensor MAX6612 detects the ambient temperature. Then the current driver delivers the appropriate amount of current (50 mA) into the auxiliary coil of the magnet. This coil can trim B_0 accordingly (75 mT/A) to compensate the shifting of B_0. Thus, a stable B_0, which is the sum of the magnetic field from the permanent magnet and the auxiliary coil, can be achieved. The injected current can be calculated from the temperature (i.e., shifting of B_0 shift from the nominal value). This calibrator allows a fix excitation frequency, which is beneficial to the robustness of the system as a POC diagnostic device.

Typically, transduction between the magnetic and voltage signals, under a static magnetic field, is the main function of solenoids [34] and spiral coils [35]. However, since B_1 should be orthogonal to B_0 [z-direction, Fig. 10(a)] for NMR experiment, B_1 has to be either in the x- or the y-direction. For solenoids and spiral coils, the circular planes of the coils need to be in the x-z plane in order to generate B_1 in the y-direction [Fig. 10(b)]. This restricts the usable space and thus the number of DMF electrodes inside the magnet since the width is 2.3x longer than the height. To resolve this, a PCB-printed butterfly-coil containing two square spiral loops connected in series with different rotation (i.e., clockwise and counter-clockwise) entails the generation of the plane-parallel B_1 (x-direction) [Fig. 10(c)]. Routed with square loops, the butterfly-coil can effectively concentrates the magnetic field between the centers of the two loops (~ 40% stronger than its circular loop counterpart). By inserting this butterfly-coil in the portable magnet (x-y plane), B_1 travels orthogonally to B_0, easing the integration of the DMF device with higher number of electrodes inside the portable magnet. Yet, as the amplitude of the μNMR signals is commensurate with B_1, the system will have a lower SNR ascribed to the lower B_1 of the butterfly-coil when compared with the spiral counterpart (0.5x). Nevertheless, the optimization of the SNRs is not only at the circuit level, but also in the co-design of the coil and RX to soothe this signal deterioration. The voltage induced on the butterfly-coil (V_{EMF}) increases with the number of turns (N) for each spiral coil attributed to the higher B_1. Yet, the thermal noise of the undesired coil resistance ($\overline{v^2_{noise,coil}}$), as depicted in Fig. 7(a), also increases with the turn's number. Together with the passive amplification network and the RX, the SNR of the output will become

$$SNR_{OUT} = \frac{V_{EMF}\sqrt{Q^2+1}}{\sqrt{(\overline{v^2_{noise,coil}}\,(Q^2+1)+\overline{v^2_{noise,LNA}})\cdot\Delta f}}$$

(4)

where the input-referred noise of the RX is assumed to be dominated by $\overline{v^2_{noise,LNA}}$ and Δf is the BW of the signal. Revealed from (4), the SNR_{OUT} is affected at both coils' geometric level (V_{EMF}, $\overline{v^2_{noise,coil}}$, and Q) and circuit
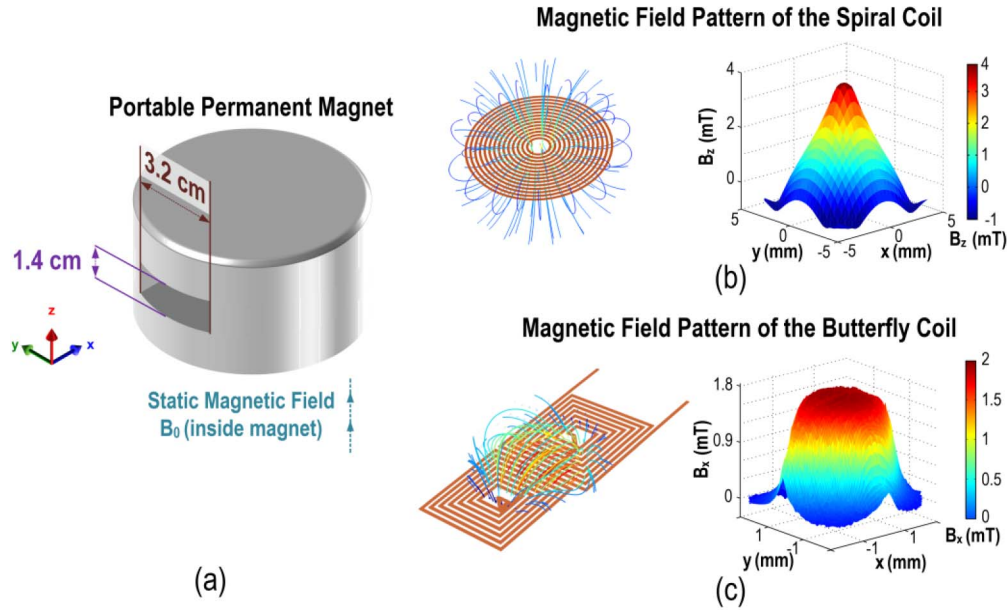
Fig. 10. (a) Geometry and limitation from the opening gap of the portable magnet. (b) & (c) The EM simulation of the magnetic field direction and strength from a spiral coil (with 14 turns) and a butterfly-coil (with 7 turns on each spiral), respectively, with a flowing current of 1 A.
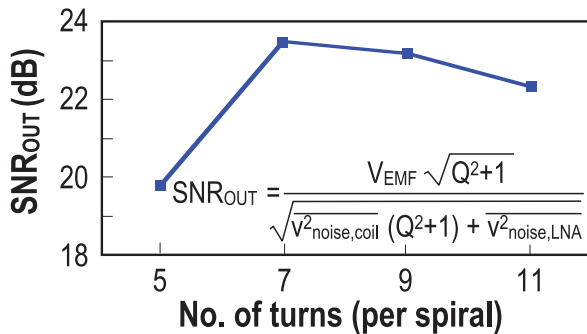

Fig. 11. Simulated SNR of the butterfly-coil-input CMOS RX with different number of turns in the coils.

level ($\overline{v^2_{noise,LNA}}$). After settling the RX noise level limited by the process and power budget, the geometry of the butterfly-coil can be finalized by performing simulation on V_{EMF}, $\overline{v^2_{noise,coil}}$, and Q with the finite element analysis software (COMSOL Multiphysics). The SNR_{OUT} maximized at 23.2 dB with 7 turns on each spiral coil (Fig. 11) is a reference value for optimization, as the magnitude of V_{EMF} will vary in practice. The dimension of the butterfly-coil is 1.0 x 0.6 cm^2 with a conductor width and space of 0.15 mm.

C. DMF Device and Its Control Circuit

To obviate laboring efforts on samples during the experiments (also the chance of sample defilement), a DMF device is introduced to enable electronic-automated sample management inside the portable magnet. When compared with the conventional channel microfluidic devices, DMF can avoid separate and complex networks of connections, laboratory gadgets such as pumps and valves and the device is reconfigurable in such a way that the droplet can move freely over a surface of electrode matrix. This DMF device is sandwiched with two glass

plates [Fig. 12(a)]. The top one with chromium plating is patterned by lithography and wet-etching to achieve customized electrodes array, followed by Ta$_2$O$_5$ and Parylene-C deposition to enhance the EWOD force. Indium tin oxide (ITO) coated on the bottom glass plate (thickness: 0.5 mm) serves as a ground plane for all electrodes. A Teflon® layer covers both plates. By utilizing the principle of EWOD, the original hydrophobic Teflon surface polarizes and becomes hydrophilic. Thus, the application of voltage signals allows the manipulation of droplets squeezed between the plates. The butterfly-coil placed underneath the thin ITO-coated glass plate of a specific electrode is the sensing site for μNMR assays. The ITO-coated substrate and electrodes designed to have minimum impact on the eddy current loss of the butterfly-coil imputed to the conductivity of the DMF device, preventing the NMR signals from deteriorating. To avoid sample evaporation and smoothen the transportation, a shell of silicone oil covers the droplets. The thickness of the ITO-coated glass can affect the B$_1$ sensitivity. From simulations, for a given power budget for the PA and LNA, a thin glass (0.1 mm) can improve the B$_1$ sensitivity by 30%. Yet, the glass becomes harder to handle and the manufacturing costs raise. To balance them, a moderate glass thickness of 0.5 mm is chosen.

To manipulate the droplets, the DMF electronic module (Fig. 4) controls the overall DMF device. A high voltage inverter (0 to 40 V) driven by an oscillator ($\sim$ 1 kHz) is utilized to generate a square wave for driving the electrodes, with the high voltage generated by a DC-DC boost converter. A capacitance-to-digital module locates the droplets, as the high permittivity water droplets (80x of air) affect the capacitance of the electrodes (C_{Elec}). A FPGA masters the operations including sample locating and transporting. This entire DMF module forms a closed-loop control of a complete automated sample management, where the FPGA controls the path of the droplets together with the operations of the
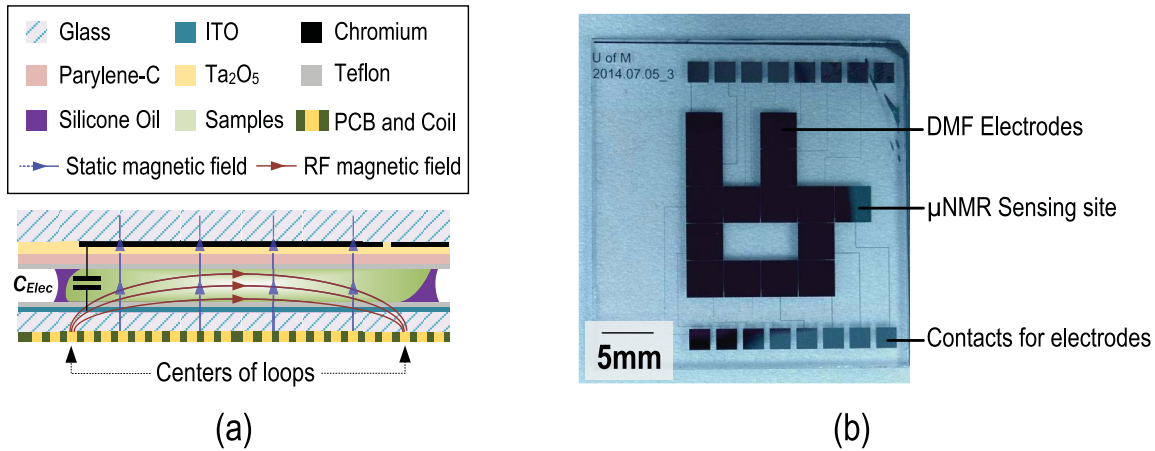
Fig. 12. (a) Assembly of the DMF device together with the butterfly-coil. The electrode and the ground plane form a capacitor C_{ELEC} with the location of the droplets revealed by the capacitance. (b) The fabricated top plane of the DMF device.

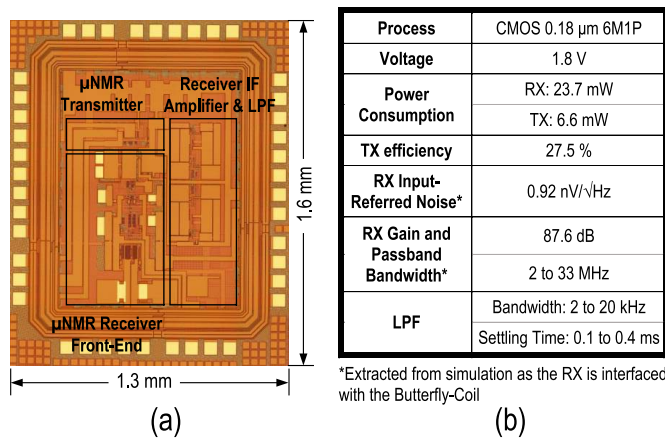Fig. 13. (a) Chip photo. (b) Measured performance summary of the μNMR TRX. The RX input-referred noise, gain, and bandwidth can only be assessed by simulations as the RX input has been tied to the butterfly-coil.

μNMR assays. To prevent crosstalk from appearing on the μNMR results, during the μNMR assay the DMF module switches off. The designed DMF device has 15 electrodes, each with 3.5 x 3.5 mm² [Fig. 12(b)]. This dimension matches with our designed butterfly-coil, benefiting the overall SNR of the system.

IV. EXPERIMENTAL RESULTS

A. Electrical Measurements

The μNMR TRX fabricated in 0.18 μm CMOS has a die area of 1.6 x 1.3 mm² dominated by the RX [Fig. 13(a)]. The operating voltage is 1.8 V and the power consumption is 6.6 mW in TX, and 23.7 mW in RX [Fig. 13(b)]. The TX has a power efficiency of 27.5%, and the effective B_1 applied to the sample is 5.3 Gauss. For the RX, the forefront LNA dominates the power consumption (68%). When the μNMR system turns off after each assay, the power consumption lowers to 100 μW. Assuming that the μNMR experiments, performed with two AA batteries and an external DC-DC converter with a 90% efficiency, are with 256 echoes and 4 ms of echoes interval (~1.1 s), they allow approximately ~1 million assays. The butterfly-coil, fabricated on the same PCB containing the
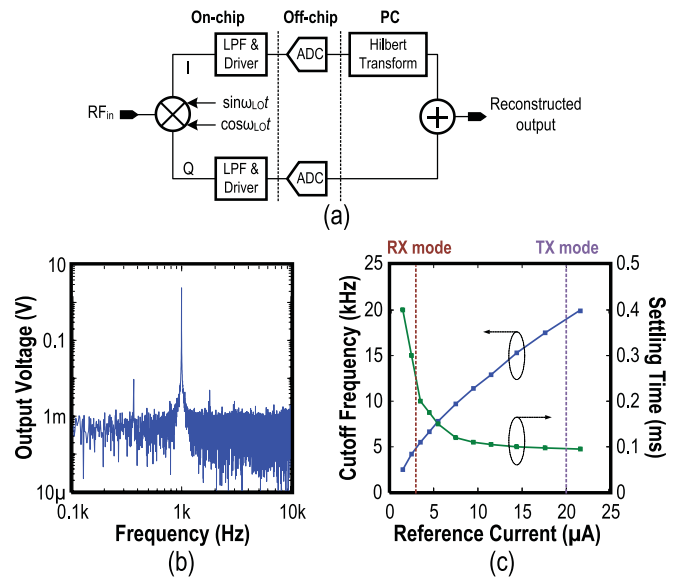

Fig. 14. (a) Block diagram of the image-reject RX. (b) Measured RX output spectrum with an externally coupled magnetic field at 19.999 MHz and a LO of 20 MHz after image noise removal. (c) Cutoff frequency and settling time of the LPF versus the bias current. Working regions of the LPF at different modes labeled.

CMOS TRX to prevent parasitics and enable a higher level of integration, measures an inductance of 373 nH with Q of 31.0 at 20 MHz.

As the TRX is linked with the butterfly-coil, the RX cannot be evaluated by typical 50 Ω equipment. To address it, another butterfly-coil (same dimension) is connected with a signal generator to couple an RF magnetic field on the original butterfly-coil (separation: 10 mm), thereby emulating the RF magnetic field induced by protons' spinning. With the external RF magnetic field with frequency of 19.999 MHz and the LO_{ref} with frequency of 80 MHz (i.e., LO for mixer at 20 MHz), signals with a frequency of 1 kHz are revealed at the quadrature outputs. The digitized I channel is processed with Hilbert transform in the digital domain (software level) to achieve a 90° phase shift [Fig. 14(a)]. The resultant signal is then added with the signal from
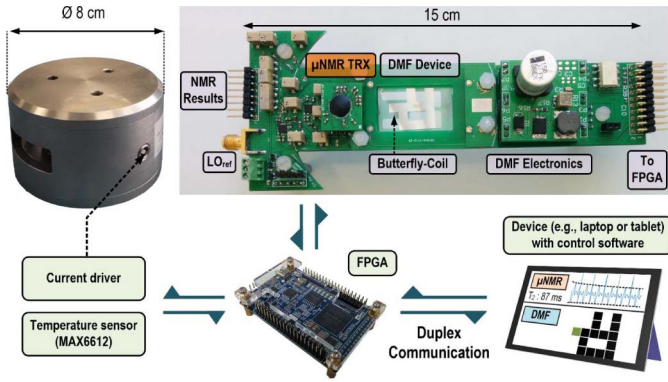
Fig. 15.   The system hardware of the μNMR system, linked with a FPGA (DE0-nano) and a program implemented in C# which facilitates the system control, result collection, and displays.

Fig. 16.   Operation of the μNMR system. (a)-(c) were taken outside the magnet for demonstration purposes only. (a) Initial position of the sample and its projected path. (b) Droplet moved to the adjacent electrode by applying voltage on it. (c) Final position (μNMR sensing site) of the droplet. (d) Measured μNMR signal from water droplet excited by CPMG pulse sequence with 256 echoes and 4 ms interval, and with the envelope extracted and fitted to a mono-exponential function, revealed in the inset.

the Q channel to achieve image rejection. The SNR of the signal improved by 40% (3 dB) after image noise removal matches with the theoretical derivation [Fig. 14(b)]. Besides, to substantiate the fact that the DMF device has negligible impact on the butterfly-coil, a repetition of the above measurements is necessary with the DMF device put atop the butterfly-coil. There is no manifest impact on the signal (both signal amplitude and SNR) at the output of the RX, validating that the DMF device is not influential on the butterfly-coil-input CMOS TRX.

Fig. 14(c) presents the f_{-3dB} and settling time (t_s, 5% from the steady state) from a step response (100 mV) of the LPF measured at different bias currents. The f_{-3dB} can be dynamically tuned from 2 to 20 kHz by switching a single bias current (from 1.5 to 21.5 μA) shared by the 3 Biquads of the LPF. Consequently, t_s of the LPF from the step response decreases from 0.4 to 0.1 ms. Thus, the RX can be set at a higher f_{-3dB} (20 kHz) to swiftly recover from the excitation pulses (t_s: 0.1 ms) in the TX mode, to facilitate a short t_{dead}. On the other hand, a lower f_{-3dB} (5 kHz) is set in the RX mode to limit the in-band noise of the RX, perceiving the contrariety between t_{dead} and in-band noise.

The measurement of B_0 of the magnet against different temperatures (calibrated inside a temperature chamber) verifies the operation of the magnetic-field calibrator. The magnetic-field stabilization scheme suppresses B_0 variation from 5.54 mT to 70 μT (3 kHz in terms of frequency) at nominal B_0 (0.458 T) with temperature variation from 18 to 30 °C. Thus, with the excitation frequency fixed at 19.5 MHz it eases the calibration of the device for POC applications.

B. System Verification

Fig. 15 illustrates the μNMR system, including the DMF device and its control circuit, integrated on a single PCB for compactness and better reproducibility. A FPGA (DE0-Nano) monitors the schedule of sample movement and μNMR-signal acquisition and digitization. A software program in C# visualizes the μNMR assays results and shows the execution status of the experimental protocol in real time. Samples are preloaded inside the DMF device before the experiment, with their transportation and mixing together with
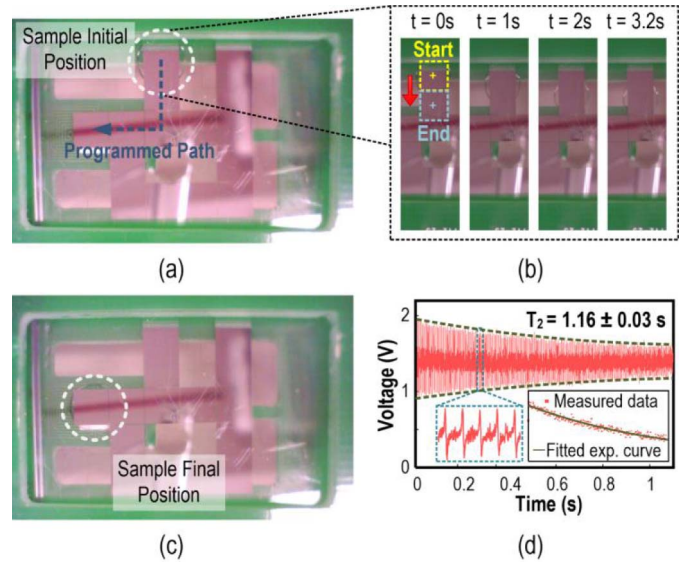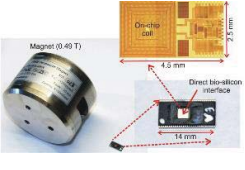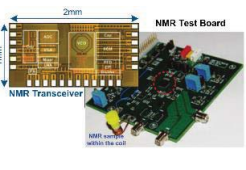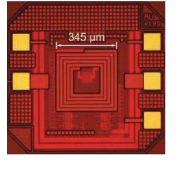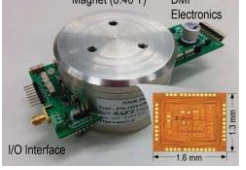
the triggering of μNMR experiments executed electronically. Fig. 16(a) exhibits an example using a water droplet (8 μL) routed to the μNMR sensing site. Fig. 16(b) shows the droplet position, detected by a capacitance-to-digital module, guided to the corresponding electrode through the application of a voltage signal progressively to achieve sample transportation with an average velocity of 1.17 mm/s. The elevation of the actuation voltage improves the velocity. Yet, this burdens the electric fields on the Ta_2O_5 layer and deteriorates the reliability of the DMF device. Thus, a moderate voltage of 40 V_{pp} was chosen as the velocity is not a critical issue for the application. To ensure successful transportation, the location of the droplets is tracked in real time. Upon arrival on the μNMR sensing site, the μNMR assay is triggered automatically [Fig. 16(c)]. The parameters of the μNMR experiment can be tuned from the program. After removing the image noise for the quadrature signals, the acquired μNMR results are analyzed and displayed in the program. The T_2 from the water droplet (1.16 ± 0.03 s) can be derived from fitting the envelope of the echoes response to a decay exponential function [Fig. 16(d)]. To enhance the SNR, the experiments are repeated 8x, and their results are averaged to suppress the background noise.

This system detects the concentration of chemical and biological targets inside the droplets. Before the assays, the samples (and probes if necessary) are loaded inside the DMF device. Afterwards, the DMF device detects the locations of the droplets, and projects the paths of the droplets adaptively to concisely transport them to the μNMR sensing site individually without the risk of fortuitous mixing [Fig. 17(a)]. When a droplet is under assay, the other droplets stay in a fix position and the DMF driving signal turns off to prevent undesired interference on μNMR signals.

TABLE III
COMPARISON WITH THE EXISTING CMOS-BASED NMR SYSTEMS

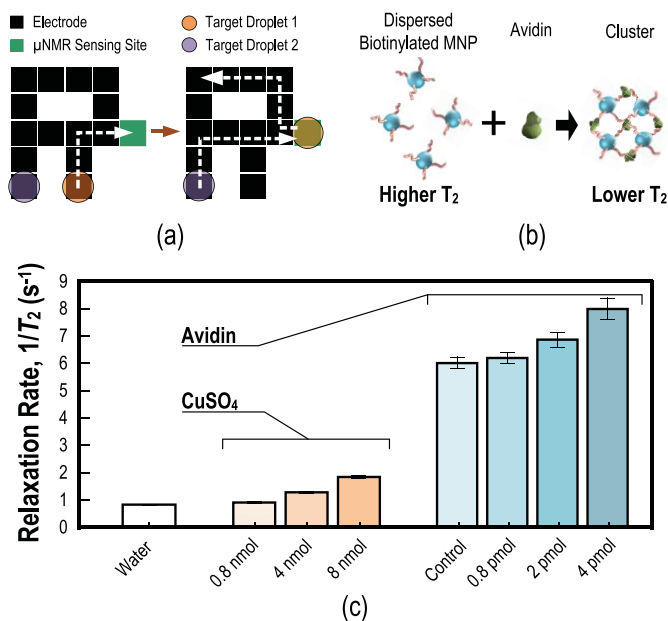|	JSSC'11 [21]	CICC'12 [34]	A-SSCC'13 [35]	This Work
System Perspective				
Functionality	Relaxometry	Spectroscopy	Microscopy	Relaxometry
Coil Style	On-chip Spiral	Off-chip Solenoid	On-chip Spiral	**Off-chip PCB Butterfly**
Magnet	Portable (1.2 kg, 0.5 T)	N/A (5 T)	Large-scale (Bruker 7 T)	Portable (1.2 kg, 0.5 T)
Sample Handling per Experiment	One	One	One	**Multiple**
Pre-/Post-Sample Reaction Supportability	No (Only μNMR)	No (Only μNMR)	No (Only μNMR)	**Yes (Mixing/Splitting + μNMR)**
Circuit Perspective				
Process (Voltage)	0.18 μm (1.8 V)	0.13 μm (1.5 V)	0.13 μm (1.5 V)	0.18 μm (1.8 V)
Operation Frequency	21 MHz	5-300 MHz	300 MHz	20 MHz
Integration Level	TRX	RX	RX	TRX
IRN (w/ & w/o coil)	0.93/1.26 nV/√Hz	--/3.5 nV/√Hz	0.26/-- nV/√Hz	**0.16/0.92 nV/√Hz**
Power	N/A	18 mW	18 mW	RX: 23.7 mW/ TX: 6.6 mW
LPF Integration	No	Yes	No	**Yes (Dynamic BW Tuning)**

Fig. 17. (a) Multi-sample management scheme for the system. The DMF device can adaptively program the path of the droplets to transport them to the μNMR sensing site for assaying. (b) Illustration of the sensing mechanism for avidin. The biotinylated MNPs, which has a higher T_2 when dispersed, form aggregates with avidin and thus enhance the magnetic field perturbation and decrease the T_2. (c) Relaxation rate ($1/T_2$) from various targets with different concentration.

By utilizing probe-decorated MNPs, this system is capable of selectively detecting the target inside the droplets. The aggregated MNPs perturb the local magnetic field homogeneity depending on the clusters size reflected from T_2 of the

samples [36]. The MNPs stay mono-dispersed without the target inside the droplets. When the targets are mixed with the probe-decorated MNPs, the MNPs form nanoparticle micro-clusters ascribed to the binding between the probe on the MNPs and target. The T_2 then decreases according to the amount of targets. To exemplify this, MNPs ([Fe] = 0.5 mM, Ø = 30 nm) coated with biotin are employed to sense the avidin inside the samples as biotin binds with avidin attributed to the low dissociation constant between them ($\sim 10^{-15}$ M). Initially, the droplets of probes and targets are placed inside the DMF device, then guided to mix with the targets (by the DMF device), and finally transported to the μNMR sensing site. Upon binding with avidin, the biotinylated MNPs cluster into aggregates [Fig. 17(b)]. The concentration of the avidin can be pinpointed from the T_2 of the samples (slope: –42.5 s^{-1}mM^{-1}; R^2: 0.993) with detection sensitivity of 0.8 pmol [Fig. 16(c)]. In addition, this system is also capable of detecting the para-magnetic copper (II) ions (from copper (II) sulfate solution) as it affects the local magnetic-field homogeneity. Consequently, the concentration of copper (II) ions is commensurate with T_2 of the water (slope: 1.05 s^{-1}mM^{-1}; R^2: 0.998) [Fig. 17(c)]. This automated assay reduces the chance of sample contamination and culminates in a high-throughput and feasible target quantification within minutes (depending on the number of droplets and paths).

C. Discussion and Outlook

Table III compares this work with other NMR platforms equipped with CMOS TRX/RX for different functionalities. Ascribed to the 2D DMF device, this μNMR system for

target pinpointing is the first platform to accomplish automated multi-sample management, which is a promising feature for POC devices [37]. This DMF device not only locates and transports the droplet to the μNMR sensing site, it also supports pre- and post-experiment processes such as mixing and splitting of the droplets for broader applications. Besides, this DMF device can be integrated with a heating module to perform thermal profiling on the samples with μNMR assay [38]. This versatility of NMR and DMF integration is tantalizing to a micro total-analysis system. Yet, the degraded sensitivity of the coil and the distance from the coil to the samples ascribed to the thickness of the DMF device worsen the SNR thus the limit-of-detection of the system. To resolve this, a complete study on the geometry of the coil (multi-layer or asymmetric spiral) and investigation on the size, magnetic core materials and valency of the MNPs can be performed to boost the limit-of-detection. Despite this, the electronic-automated sample μNMR assay still renders the proposed platform as a promising tool for POC applications.

V. Conclusions

A μNMR CMOS TRX for biological/chemical assays has been co-developed with a glass-substrate DMF device for electronic-automated sample management plus relaxometry measurement. To facilitate their integration inside a space-limited portable magnet, a butterfly-coil input has been introduced. It allows the TRX to transduce magnetic signals from nuclei spins into voltage signals without physically contacting the samples (i.e., non-invasive), or affecting the sample movement managed by the DMF device (i.e., fully compatible). The TRX primarily includes: 1) a TX consisting of a pulse-sequence synthesizer together with an inverter-based PA to excite the protons; 2) a RX consisting of a multi-stage NMOS-PMOS differential-pair LNA, an active double-balance quadrature mixer, and a source-follower-based dynamic-baseband-BW 6th-order Butterworth LPF that culminates in low in-band noise in the RX mode, and short dead-time in the TX mode to process the μNMR signals with negligible distortion. The μNMR experiments evince the functionality of this system from the μNMR experiments with copper (II) ions and avidin detection with biotinylated MNPs by measuring T_2 of the samples.

References

[1] P. Yager *et al.*, "Microfluidic diagnostic technologies for global public health," *Nature*, vol. 442, pp. 412–418, Jul. 2006.

[2] A. Niemz, T. M. Ferguson, and D. S. Boyle, "Point-of-care nucleic acid testing for infectious diseases," *Trends Biotechnol.*, vol. 29, no. 5, pp. 240–250, May 2011.

[3] P. K. Drain *et al.*, "Diagnostic point-of-care tests in resource-limited settings," *Lancet Infectious Diseases*, vol. 14, no. 3, pp. 239–249, Mar. 2014.

[4] G. Gauglitz, "Point-of-care platforms," *Annu. Rev. Anal. Chem.*, vol. 7, pp. 297–315, Jun. 2014.

[5] H. M. Jafari, K. Abdelhalim, L. Soleymani, E. H. Sargent, S. O. Kelley, and R. Genov, "Nanostructured CMOS wireless ultra-wideband label-free PCR-free DNA analysis SoC," *IEEE J. Solid-State Circuits*, vol. 49, no. 5, pp. 1223–1241, May 2014.

[6] Y.-J. Huang *et al.*, "A self-powered CMOS reconfigurable multi-sensor SoC for biomedical applications," *IEEE J. Solid-State Circuits*, vol. 49, no. 4, pp. 851–866, Apr. 2014.

[7] K.-H. Lee, S. Choi, J. O. Lee, J.-B. Yoon, and G.-H. Cho, "CMOS capacitive biosensor with enhanced sensitivity for label-free DNA detection," in *IEEE Int. Solid-State Circuits Conf. Dig. Tech. Papers*, Feb. 2012, pp. 120–121.

[8] E. Ghafar-Zadeh and M. Sawan, *CMOS Capacitive Sensors for Lab-on-Chip Applications: A Multidisciplinary Approach*, La Vergne, TN, USA: Springer, 2010.

[9] D. E. Schwartz, P. Gong, and K. L. Shepard, "Time-resolved Förster-resonance-energy-transfer DNA assay on an active CMOS microarray," *Biosensors Bioelectron.*, vol. 24, no. 3, pp. 383–390, Nov. 2008.

[10] B. Jang, P. Cao, A. Chevalier, A. Ellington, and A. Hassibi, "A CMOS fluorescent-based biosensor microarray," in *IEEE Int. Solid-State Circuits Conf. Dig. Tech. Papers*, Feb. 2009, pp. 436–437.

[11] R. Thewes, "Introduction to CMOS-based DNA microarrays," in *Smart Sensor Systems: Emerging Technologies and Applications*, G. Meijer, K. Makinwa and M. Pertijs, Eds. London, U.K.: Wiley, 2014, pp. 145–172.

[12] P.-H. Kuo *et al.*, "A smart CMOS assay SoC for rapid blood screening test of risk prediction," in *IEEE Int. Solid-State Circuits Conf. Dig. Tech. Papers*, Feb. 2015, pp. 390–391.

[13] A. Pai, A. Khachaturian, S. Chapman, A. Hu, H. Wang, and A. Hajimiri, "A handheld magnetic sensing platform for antigen and nucleic acid detection," *Analyst*, vol. 139, no. 6, pp. 1403–1411, Mar. 2014.

[14] D. A. Hall, R. S. Gaster, K. A. A. Makinwa, S. X. Wang, and B. Murmann, "A 256 pixel magnetoresistive biosensor microarray in 0.18 μm CMOS," *IEEE J. Solid-State Circuits*, vol. 48, no. 5, pp. 1290–1301, May 2013.

[15] Y.-J. Huang *et al.*, "A CMOS cantilever-based label-free DNA SoC with improved sensitivity for hepatitis B virus detection," *IEEE Trans. Biomed. Circuits Syst.*, vol. 7, no. 6, pp. 820–831, Dec. 2013.

[16] H.-H. Tsai *et al.*, "Multiple type biosensors fabricated using the CMOS BioMEMS platform," *Sens. Actuators B, Chem.*, vol. 144, no. 2, pp. 407–412, Feb. 2010.

[17] L. Josephson, J. M. Perez, and R. Weissleder, "Magnetic nanosensors for the detection of oligonucleotide sequences," *Angew. Chem. Int. Ed.*, vol. 113, no. 17, pp. 3304–3306, Sep. 2001.

[18] J. M. Perez, L. Josephson, T. O'Loughlin, D. Högemann, and R. Weissleder, "Magnetic relaxation switches capable of sensing molecular interactions," *Nature Biotechnol.*, vol. 20, no. 8, pp. 816–820, Aug. 2002.

[19] J. M. Perez, F. J. Simeone, Y. Saeki, L. Josephson, and R. Weissleder, "Viral-induced self-assembly of magnetic nanoparticles allows the detection of viral particles in biological media," *J. Amer. Chem. Soc.*, vol. 125, no. 34, pp. 10192–10193, Aug. 2003.

[20] J. Grimm, J. M. Perez, L. Josephson, and R. Weissleder, "Novel nanosensors for rapid analysis of telomerase activity," *Cancer Res.*, vol. 64, no. 2, pp. 639–643, Jan. 2004.

[21] N. Sun, T.-J. Yoon, H. Lee, W. Andress, R. Weissleder, and D. Ham, "Palm NMR and 1-chip NMR," *IEEE J. Solid-State Circuits*, vol. 46, no. 1, pp. 342–352, Jan. 2011.

[22] N. Sun, Y. Liu, H. Lee, R. Weissleder, and D. Ham, "CMOS RF biosensor utilizing nuclear magnetic resonance," *IEEE J. Solid-State Circuits*, vol. 44, no. 5, pp. 1629–1643, May 2009.

[23] N. Sun and D. Ham, "Hardware developments: Handheld NMR systems for biomolecular sensing," in *Mobile NMR and MRI: Developments and Applications*, M. L. Johns, E. O. Fridjonsson, S. J. Vogt and A. Haber, Eds. London, U.K.: The Royal Society of Chemistry, 2015, pp. 158–182.

[24] D. Ha, J. Paulsen, N. Sun, Y.-Q. Song, and D. Ham, "Scalable NMR spectroscopy with semiconductor chips," *Proc. Nat. Acad. Sci.*, vol. 111, no. 33, pp. 11955–11960, Aug. 2014.

[25] J. Gao *et al.*, "An intelligent digital microfluidic system with fuzzy-enhanced feedback for multi-droplet manipulation," *Lab Chip*, vol. 13, no. 3, pp. 443–451, Feb. 2013.

[26] K.-M. Lei, P.-I. Mak, M.-K. Law, and R. P. Martins, "A palm-size μNMR relaxometer using a digital microfluidic device and a semiconductor transceiver for chemical/biological diagnosis," *Analyst*, vol. 140, no. 15, pp. 5129–5137, Aug. 2015.

[27] I. Swyer, R. Soong, M. Dryden, A. Simpson, and A. Wheeler, "Interfacing digital microfluidics to high-field nuclear magnetic spectroscopy," in *Proc. 19th Int. Conf. Miniaturized Syst. Chem. Life Sci. (MicroTAS)*, Oct. 2015, pp. 296–298.

[28] K.-M. Lei, P.-I. Mak, M.-K. Law, and R. P. Martins, "A μNMR CMOS transceiver using a butterfly-coil input for integration with a digital microfluidic device inside a portable magnet," in *Proc. IEEE Asian Solid-State Circuits Conf. (A-SSCC)*, Nov. 2015, pp. 1–4.

[29] H. Y. Carr and E. M. Purcell, "Effects of diffusion on free precession in nuclear magnetic resonance experiments," *Phys. Rev.*, vol. 94, no. 3, pp. 630–638, May 1954.

[30] S. Meiboom and D. Gill, "Modified spin-echo method for measuring nuclear relaxation times," *Rev. Sci. Instrum.*, vol. 29, no. 8, pp. 688–691, Aug. 1958.

[31] S. D'Amico, M. Conta, and A. Baschirotto, "A 4.1-mW 10-MHz fourth-order source-follower-based continuous-time filter with 79-dB DR," *IEEE J. Solid-State Circuits*, vol. 41, no. 12, pp. 2713–2719, Dec. 2006.

[32] T.-T. Zhang *et al.*, "15-nW biopotential LPFs in 0.35-μm CMOS using subthreshold-source-follower biquads with and without gain compensation," *IEEE Trans. Biomed. Circuits Syst.*, vol. 7, no. 5, pp. 690–702, Oct. 2013.

[33] J. Watzlaw, S. Glöggler, B. Blümich, W. Mokwa, and U. Schnakenberg, "Stacked planar micro coils for single-sided NMR applications," *J. Magn. Reson.*, vol. 230, pp. 176–185, May 2013.

[34] J. Kim, B. Hammer, and R. Harjani, "A 5–300 MHz CMOS transceiver for multi-nuclear NMR spectroscopy," in *Proc. IEEE Custom Integr. Circuits Conf. (CICC)*, Sep. 2012, pp. 1–4.

[35] J. Anders, J. Handwerker, M. Ortmanns, and G. Boero, "A fully-integrated detector for NMR microscopy in 0.13 μm CMOS," in *Proc. IEEE Asian Solid-State Circuits Conf. (A-SSCC)*, Nov. 2013, pp. 437–440.

[36] C. Min, H. Shao, M. Liong, T.-J. Yoon, R. Weissleder, and H. Lee, "Mechanism of magnetic relaxation switching sensing," *ACS Nano*, vol. 6, no. 8, pp. 6821–6828, Aug. 2012.

[37] V. Gubala, L. F. Harris, A. J. Ricco, M. X. Tan, and D. E. Williams, "Point of care diagnostics: Status and future," *Anal. Chem.*, vol. 84, no. 2, pp. 487–515, Jan. 2012.

[38] P. Y. Keng *et al.*, "Micro-chemical synthesis of molecular probes on an electronic microfluidic device," *Proc. Nat. Acad. Sci. (PNAS)*, vol. 109, no. 3, pp. 690–695, Jan. 2012.

Pui-In Mak (S'00–M'08–SM'11) received the Ph.D. degree from the University of Macau (UM), Macao, China, in 2006.

He is currently an Associate Professor with the UM Faculty of Science and Technology–ECE, and Associate Director (Research) at the UM State Key Laboratory of Analog and Mixed-Signal VLSI. His research interests are in analog and radio-frequency (RF) circuits and systems for wireless, biomedical, and physical chemistry applications. His group contributed 10 state-of-the-art chips at recent ISSCCs: software-defined radios, ultra-low-power radios, micro-power amplifiers, a ring oscillator, and the micro-NMR platform. His team also pioneered the world's-first *Intelligent Digital Microfluidic Technology (iDMF)* with micro-Nuclear Magnetic Resonance (μNMR) and polymerase chain reaction (PCR) capabilties. He has co-authored three books: *Analog-Baseband Architectures and Circuits for Multistandard and Low-Voltage Wireless Transceivers* (Springer, 2007), *High-/Mixed-Voltage Analog and RF Circuit Techniques for Nanoscale CMOS* (Springer, 2012), and *Ultra-Low-Power and Ultra-Low-Cost Short-Range Wireless Receivers in Nanoscale CMOS* (Springer, 2015).

Prof. Mak was a co-recipient of the DAC/ISSCC Student Paper Award 2005, CASS Outstanding Young Author Award 2010, SSCS Pre-Doctoral Achievement Awards 2014 and 2015, A-SSCC Distinguished Design Award 2015; ISSCC Silkroad Award 2016, the National Scientific and Technological Progress Award 2011, and the Best Associate Editor of IEEE TRANSACTIONS ON CIRCUITS AND SYSTEMS II 2012–2013. In 2005, he was decorated with the Honorary Title of Value for scientific merits by the Macau Government. His involvements with IEEE are: Editorial Board Member of IEEE Press (2014–2016); IEEE Distinguished Lecturer (2014–2015); Member of Board-of-Governors of IEEE Circuits and Systems Society (2009–2011); Senior Editor of IEEE JOURNAL ON EMERGING AND SELECTED TOPICS IN CIRCUITS AND SYSTEMS (2014–2015); Guest Editor of IEEE RFIC VIRTUAL JOURNAL (2014); Associate Editor of IEEE TRANSACTIONS ON CIRCUITS AND SYSTEMS I (2010–2011, 2014–2015) and II (2010–2013). He is the TPC Vice Co-Chair of ASP-DAC'16, and currently a TPC member of ISSCC, ESSCIRC, and A-SSCC.

Ka-Meng Lei (S'12) received the B.Sc. degree in electrical and electronics engineering from the University of Macau, Macao, China, in 2012. Currently, he is working toward the Ph.D. degree in electrical and computer engineering in the State Key Laboratory of Analog and Mixed-Signal VLSI (SKL-AMSV) and FST-ECE, University of Macau.

He worked as a trainee to develop a video de-interlacing processor at Evatronix IP, Gliwice, Poland, in the summer of 2012. He is now a research assistant in SKL-AMSV working on CMOS micro-NMR biosensor. His research interests include sensors and analog front-end interfaces, analog circuit techniques for micro-NMR, intelligent digital microfluidics platform, and system planning, integration, and optimization for biomedical devices.

Mr. Lei was a co-recipient of the ChipIdea Microelectronics Prize (Bachelor level) 2012, Best Paper Award in Asia Symposium on Quality Electronic Design 2013, Student/Young Researcher Grant from the Chemical and Biological Microsystems Society 2015, Distinguished Design Award of the Student Design Contest of IEEE Asian Solid-State Circuits Conference 2015, and the Silkroad Award of the IEEE International Solid-State Circuits Conference 2016.

Man-Kay Law (M'11) received the B.Sc. degree in computer engineering and the Ph.D. degree in electronic and computer engineering from Hong Kong University of Science and Technology (HKUST), in 2006 and 2011, respectively. During his Ph.D. study, he performed research on ultra-low power/energy harvesting CMOS sensor designs for wireless sensing platforms.

In February 2011, he joined HKUST as a Visiting Assistant Professor. He is currently an Assistant Professor in the State Key Laboratory of Analog and Mixed-Signal VLSI, Faculty of Science and Technology, University of Macau, Macao. His research interests are in the development of ultra-low power/energy harvesting and sensing circuits for wireless sensing and biomedical systems, specializing in smart CMOS temperature sensors, CMOS image sensors, ultra-low power analog design techniques, and integrated energy harvesting techniques. Related applications include RFID with embedded sensors, energy harvesting systems and passively powered biomedical implants.

Dr. Law serves as a member of the IEEE Circuits and Systems Society (CASS) committee on Sensory Systems as well as Biomedical Circuits and Systems.

Rui P. Martins (M'88–SM'99–F'08) was born on April 30, 1957. He received the Bachelor (5-years), Masters, and Ph.D. degrees, as well as the *Habilitation* for Full Professor in electrical engineering and computers from the Department of Electrical and Computer Engineering, Instituto Superior Técnico (IST), TU of Lisbon, Portugal, in 1980, 1985, 1992, and 2001, respectively.

He has been with the Department of Electrical and Computer Engineering (DECE)/IST, TU of Lisbon, since October 1980. Since 1992, he has been on leave from IST, TU of Lisbon, and with the Department of Electrical and Computer Engineering, Faculty of Science and Technology (FST), University of Macau (UM), Macao, China, where he has been a Full Professor since 1998. In FST he was the Dean of the Faculty from 1994 to 1997, and he has been Vice-Rector of the University of Macau since 1997. From September 2008, after the reform of the UM Charter, he was nominated after open international recruitment as Vice-Rector (Research) until August 31, 2013. Within the scope of his teaching and research activities he has taught 21 bachelor and master courses and has supervised (or co-supervised) 26 theses, Ph.D. (11) and Masters (15). He has published: 12 books, co-authoring 5 and co-editing 7, plus 5 book chapters; 266 refereed papers, in scientific journals (60) and in conference proceedings (206); and 70 other academic works, in total 348 publications. He has also co-authored 7 U.S. patents. He also created the *Analog and Mixed-Signal VLSI Research Laboratory of UM*: http://www.fst.umac.mo/en/lab/ans_vlsi/website/index.html, elevated in January 2011 to State Key Lab of China (the first in Engineering in Macao), being its Founding Director.

Prof. Martins was the Founding Chairman of the IEEE Macau Section from 2003 to 2005, and of the IEEE Macau Joint Chapter on Circuits and Systems (CAS)/Communications (COM) from 2005 to 2008 [2009 *World Chapter of the Year* of the IEEE Circuits And Systems Society (CASS)]. He was the General Chair of the 2008 IEEE Asia-Pacific Conference on Circuits and Systems, *APCCAS'2008*, and was the Vice-President for the Region 10 (Asia, Australia, and the Pacific) of the IEEE CASS for 2009–2011. He was also the Vice-President (World) Regional Activities and Membership of the IEEE CASS for 2012–2013. He was Associate Editor of the IEEE Transactions on Circuits and Systems II: Express Briefs 2010–2013. He is also a member of the IEEE CASS Fellow Evaluation Committee (Class of 2013). He received two government decorations: the Medal of Professional Merit from the Macao Government (Portuguese Administration) in 1999, and the Honorary Title of Value from Macao SAR Government (Chinese Administration) in 2001. In July 2010 he was elected unanimously as Corresponding Member of the Portuguese Academy of Sciences (in Lisbon), being the only Portuguese academician living in Asia.